

**SPLIT-BEAM ECHOSOUNDER OBSERVATIONS OF NATURAL  
METHANE SEEP VARIABILITY IN THE NORTHERN GULF OF MEXICO**

**BY**

**KEVIN W. JERRAM**

*B.S. Mechanical Engineering, University of New Hampshire, 2007*

**THESIS**

**Submitted to the University of New Hampshire  
in Partial Fulfillment of  
the Requirements for the Degree of**

**Master of Science  
in  
Ocean Engineering**

**May, 2014**

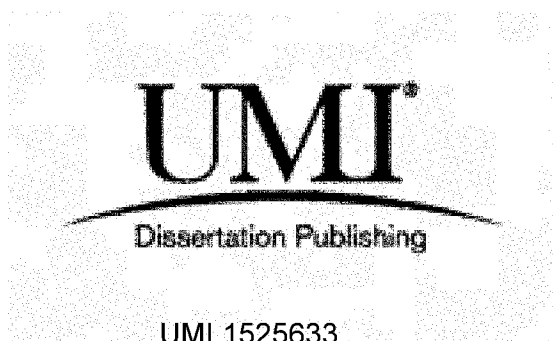
UMI Number: 1525633

All rights reserved

INFORMATION TO ALL USERS

The quality of this reproduction is dependent upon the quality of the copy submitted.

In the unlikely event that the author did not send a complete manuscript and there are missing pages, these will be noted. Also, if material had to be removed, a note will indicate the deletion.

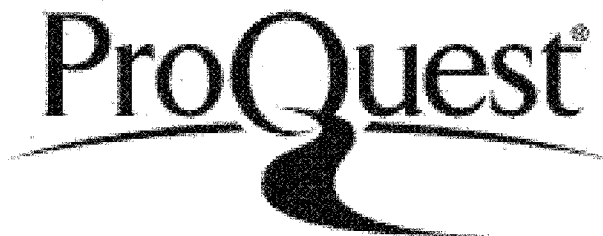


UMI 1525633

Published by ProQuest LLC 2014. Copyright in the Dissertation held by the Author.

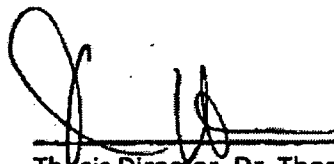
Microform Edition © ProQuest LLC.

All rights reserved. This work is protected against unauthorized copying under Title 17, United States Code.

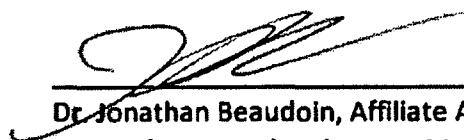


ProQuest LLC  
789 East Eisenhower Parkway  
P.O. Box 1346  
Ann Arbor, MI 48106-1346

This thesis has been examined and approved.



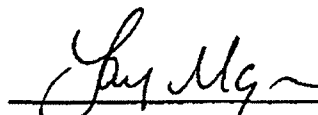
Thesis Director, Dr. Thomas Weber, Assistant Professor  
Mechanical Engineering



Dr. Jonathan Beaudoin, Affiliate Assistant Professor  
Center for Coastal and Ocean Mapping



Dr. Brian Calder, Research Associate Professor, Associate Director  
Center for Coastal and Ocean Mapping



Dr. Larry Mayer, Director  
Center for Coastal and Ocean Mapping

05/02/2014

Date

## ACKNOWLEDGEMENTS

This work was supported by the National Oceanic and Atmospheric Administration's (NOAA) Office of Coast Survey and Office of Exploration and Research through grants NA05NOS4001153 and NA10NOS4000073. The author would like to thank the captain, crew, and scientific personnel of NOAA Ship *Okeanos Explorer* for their efforts during data collection. Additionally, the author thanks Rick Towler (NOAA Alaska Fisheries Science Center) and Dezhang Chu (NOAA Northwest Fisheries Science Center) for providing software to parse Simrad EK60 raw data files and to calculate calibration sphere target strength, respectively. Finally, the author thanks his lovely partner, Allison, for her unwavering support throughout this research.

## TABLE OF CONTENTS

ACKNOWLEDGEMENTS .....	iii
LIST OF TABLES .....	v
LIST OF FIGURES .....	vi
ABSTRACT .....	vii
CHAPTER .....	PAGE
INTRODUCTION .....	1
I. METHODS .....	3
Data Collection .....	5
Calibration .....	6
Positioning and Profiling .....	7
Timing .....	9
Determination of SBES Angular Offsets .....	10
Seep Clustering .....	11
TS of Seep Targets .....	12
$S_z$ for Single Discrete Plumes .....	14
Diffuse and Multiple Discrete Plumes .....	16
II. RESULTS .....	17
Seep Observations and Positions .....	17
$S_z$ Profiles and Plume Depths .....	20
III. DISCUSSION .....	25
Seep Positioning and Clustering .....	25
Plume Observations and $S_z$ Profiles .....	28
$S_z$ Base Variability .....	30
IV. CONCLUSIONS .....	33
LIST OF REFERENCES .....	35
APPENDIX – MATLAB CODE FOR SEEP PROCESSING .....	39

## LIST OF TABLES

TABLE 1. SURVEY PASS INFORMATION .....	4
TABLE 2. SEEP OBSERVATION CLUSTERING RESULTS.....	18

## LIST OF FIGURES

FIGURE 1. OVERVIEW OF SEEP STUDY AREA AND SURVEY LINES .....	3
FIGURE 2. EXAMPLE OF SPLIT-BEAM ECHOSOUNDER RAW DATA.....	5
FIGURE 3. EXAMPLE OF MINIMUM PLUME DEPTH ESTIMATE.....	9
FIGURE 4. SCATTERING STRENGTHS OF METHANE GAS BUBBLES.....	14
FIGURE 5. GEOMETRY OF PLUME AXIS ENSONIFICATION.....	15
FIGURE 6. SEEP POSITIONING ACCURACY COMPARISON .....	19
FIGURE 7. EXAMPLE OF PLUME SCATTERING STRENGTH AND NOISE PROFILES ..	21
FIGURE 8. DISTRIBUTION OF MINIMUM OBSERVED PLUME HEIGHTS .....	22
FIGURE 9. PLUME BASE SCATTERING STRENGTHS FOR ALL OBSERVATIONS.....	24
FIGURE 10. SEEP DATA PROCESSING WORKFLOW.....	40

## ABSTRACT

# SPLIT-BEAM ECHOSOUNDER OBSERVATIONS OF NATURAL METHANE SEEP VARIABILITY IN THE NORTHERN GULF OF MEXICO

by

Kevin W. Jerram

University of New Hampshire, May, 2014

A method for positioning and characterizing marine gas seeps using an 18-kHz scientific split-beam echosounder (SBES) was developed and applied to SBES data collected in the northern Gulf of Mexico. A total of 161 plumes of presumed methane gas bubbles originating at approximately 1400 m depth were observed over 27 repeat surveys and grouped by proximity into 35 clusters. Profiles of mean target strength per vertical meter were calculated with compensation for SBES beam pattern and geometry of plume axis ensonification. These profiles were used as indicators of the fluxes and fates of gas bubbles acoustically observable at 18 kHz and showed significant variability between repeat observations at time intervals of 1 hour to 7.5 months. The minimum depths of acoustic plume observations averaged 875 m and frequently coincided with increased reverberation in layers of biological scatterers. Minimum depth estimates were limited by the SBES beam pattern in five instances.



## INTRODUCTION

Marine methane gas seeps provide nutrients for diverse biological communities on the seafloor; indicate locations of potentially exploitable hydrocarbon deposits; increase localized concentrations of dissolved methane in the water column; and, in cases of free gas ebullition and bubble ascent through the water column, contribute directly to the atmospheric quantity of this potent greenhouse gas [1]–[6]. Accordingly, interest in marine methane gas seeps from public, scientific, environmental, and governmental groups has increased significantly in recent decades [1], [7]. Of widespread and long-term interest are the locations of vent sites, the quantities and fates of free gas bubbles in the water column, and the variability of seep activity at sites of active venting [1], [8], [9].

Ship-based acoustic methods are well suited for detecting midwater plumes of gas bubbles (e.g., [5]), locating corresponding vent sites on the seafloor [10], and estimating the shallowest depths of bubble survival. Acoustic methods offer advantages over gas flux measurement systems requiring *in situ* bubble monitoring or collection equipment (e.g., [11]) in that echosounders may be readily applied over large spatial scales and do not affect gas or water flow at the seafloor [4]. Natural methane seeps have been detected and investigated with acoustic techniques in every major ocean on Earth [4] using various combinations of split-beam scientific echosounders (SBES) (e.g., [8]), multibeam echosounders (MBES) (e.g., [12]), sidescan sonars (e.g., [13]), sub-bottom profilers (e.g., [14]), and acoustic Doppler current profilers (e.g., [15]). SBES systems have also been used for detecting and monitoring anthropogenic seeps including methane gas and oil released into the water column from leaking wells and pipelines [16]–[18].

In this study, an 18-kHz Simrad EK60 SBES was utilized for detection, georeferencing, and target strength (TS) characterization of marine gas seeps in the northern Gulf of Mexico. SBES systems have been traditionally employed in fishery research, for which standard methods of *in situ* beam pattern measurements have been developed that enable calibrated TS measurements. Calibrated TS

measurements for gas bubbles are necessary to accurately calculate the bubbles' acoustic scattering cross sections, which depend primarily on gas composition, bubble radius, and ambient conditions [19]. Given information or assumptions about gas composition, distribution of bubble radii, and ambient conditions, calibrated TS measurements facilitate calculation or estimation of gas flux. In this regard, SBES systems offer the significant advantage of calibrated TS measurement over other echosounders.

The advantages of using a SBES for seep investigation were identified by Artemov [10] and addressed in part for studies with a Simrad EK500, precursor to the EK60, in the Black Sea. The method described herein is similar to that described by Artemov [9] but also incorporates several distinct features with regard to georeferencing seep targets, characterizing the scattering strength profiles of plumes, and establishing the limits of the echosounder field of view (FOV). This method was applied to SBES data collected during repeat seep surveys in an area of active venting in 2011 and 2012 to evaluate the variability in observations of gas flux and bubble fate, including presence and absence of plumes with consideration for the echosounder FOV. These results demonstrate the applicability of SBES systems for seep positioning and gas flow monitoring. Of interest for broader seep mapping efforts, the results strongly suggest that single-pass surveys do not capture the variability of gas flow from individual seep sites and that long-term flux estimates would benefit from repeat surveys.

## CHAPTER I

### METHODS

An 18-kHz Simrad EK60 SBES with 4-ms transmit pulse length and a measured -3 dB two-way (transmit and receive) beamwidth of  $12^\circ$  was used to collect water column backscatter data during seep mapping surveys aboard NOAA ship *Okeanos Explorer* over the southwest edge of the Biloxi Dome in the northern Gulf of Mexico, a region well known for gas venting [7], [20] (Fig. 1).

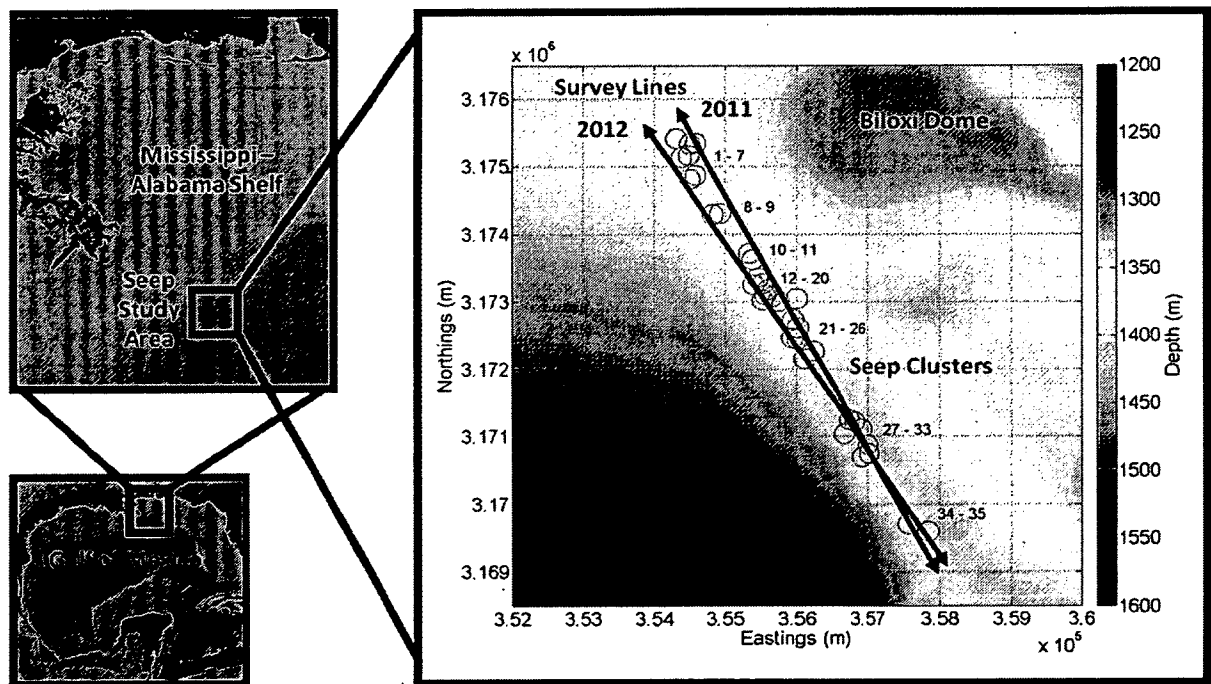


FIGURE 1. Seep study area on the southwest edge of the Biloxi Dome in the northern Gulf of Mexico. Projection is UTM (zone 16 North) referenced to the WGS84 ellipsoid. Bathymetric data were collected with a 30-kHz Kongsberg EM302 MBES aboard NOAA Ship *Okeanos Explorer* during SBES data collection in 2011. The survey lines represent the mean ship tracks during data collection in 2011 and 2012. Clusters are numbered sequentially from northwest to southeast and indicated by circles with radii of 145 m to represent the approximate SBES beamwidth footprint on the seafloor. Circles are centered at the means of seep positions for each cluster. Gulf of Mexico maps on left adapted from NOAA image ([http://www.ngdc.noaa.gov/mgg/image/gom\\_hillshade.jpg](http://www.ngdc.noaa.gov/mgg/image/gom_hillshade.jpg)).

The SBES transducer was mounted on a hull 'blister' designed for acoustic sensors at approximately 4.6 m depth. Twenty-seven survey passes over the Biloxi Dome were conducted on NNW and SSE headings, primarily as repeat lines on NNW headings during 13 passes in late August and early September 2011 and reciprocal lines on alternating headings during 14 passes in April 2012 (Table 1). Intervals between pass start times varied from less than an hour to over a week during the 2011 survey. Survey operations in 2012 were broken into two sessions separated by approximately 12 hours, with mean intervals of 1.2 hr and 1.7 hr for the first and second sessions, respectively. In order to improve SBES coverage of seeps observed during offset and orthogonal survey lines in 2011, the mean survey trackline orientation was adjusted from 152°-332° in 2011 to 147°-327° in 2012 (Fig. 1). Additionally, to increase the number of pings containing plume data at each seep site, mean vessel speed during survey operations was reduced from 11.3 kn in 2011 to 10.0 kn and 7.0 kn during the first and second sessions, respectively, in 2012.

TABLE 1. Survey pass number, start time, interval between start times (hours), heading, and speed (kn).

Pass		Start Time	Interval	Heading	Speed
1	2011	26-Aug 17:13	--	NNW	11.6
2		26-Aug 20:06	2.9	NNW	11.8
3		26-Aug 22:35	2.5	NNW	11.7
4		27-Aug 03:32	5.0	NNW	11.8
5		27-Aug 05:20	1.8	NNW	11.7
6		27-Aug 07:09	1.8	NNW	11.8
7		27-Aug 08:47	1.6	NNW	11.1
8		27-Aug 10:39	1.9	NNW	10.8
9		27-Aug 20:35	9.9	NNW	10.9
10		27-Aug 21:19	0.7	SSE	10.7
11		28-Aug 00:00	2.7	NNW	11.2
12		30-Aug 14:27	62.4	NNW	10.6
13		09-Sep 14:31	240.1	SSE	11.8
14	2012	13-Apr 04:07	5197.6	NNW	10.1
15		13-Apr 05:17	1.2	SSE	10.0
16		13-Apr 06:35	1.3	NNW	10.0
17		13-Apr 07:43	1.1	SSE	9.9
18		13-Apr 08:59	1.3	NNW	10.0
19		13-Apr 10:06	1.1	SSE	10.1
20		13-Apr 22:29	12.4	NNW	10.0
21		13-Apr 23:38	1.1	SSE	9.7
22		14-Apr 00:55	1.3	NNW	6.1
23		14-Apr 02:48	1.9	SSE	6.0
24		14-Apr 04:43	1.9	NNW	5.9
25		14-Apr 06:37	1.9	SSE	5.8
26		14-Apr 08:30	1.9	NNW	6.2
27		14-Apr 10:20	1.8	SSE	6.1

## Data Collection

The SBES data collected include TS uncorrected for transducer beam pattern and digitized electrical phase differences in the alongship and athwartship directions (Fig. 2). Vessel position and attitude were measured with an Applanix POS/MV 320 motion sensor receiving position corrections from a C-NAV 2050 differential global positioning system (GPS), yielding position and attitude uncertainties of 1.3 m (horizontal dilution of precision) and 0.02 degrees (1 standard deviation), respectively.

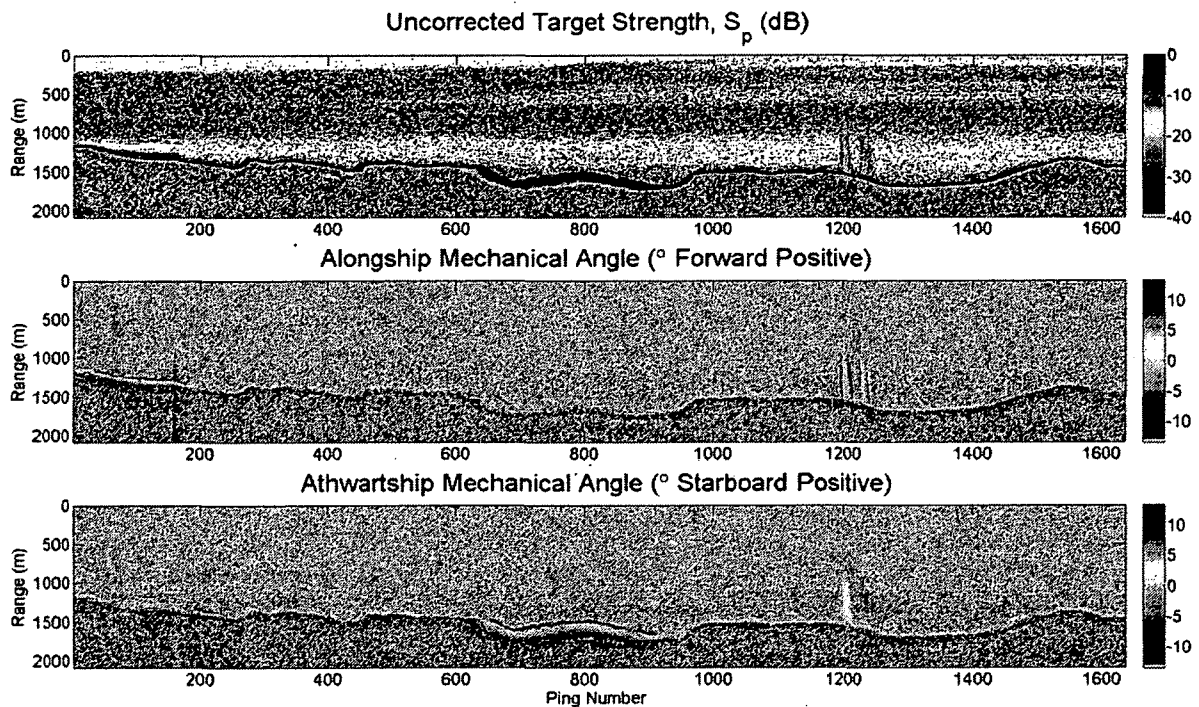


FIGURE 2. SBES data collected during seep investigation included TS uncorrected for beam pattern (top) and mechanical target angles in the alongship (middle) and athwartship (bottom) directions. Data are plotted versus range (vertical axis) and ping number (horizontal axis). Example data include interference (near ping 175) and two seep observations (near pings 1200 and 1250). Each seep observation is characterized by anomalously high scattering strength (top), progression of alongship target angles from ahead to astern (middle), and small changes in athwartship target angle (bottom). The seafloor varies between 1200 and 1700 m in this example. Two scattering layers are visible in the uncorrected TS data: one deeper scattering layer at a range of approximately 750 m and one shallower scattering layer which migrates upward from approximately 500 m to 250 m between ping numbers 400-1000 (corresponding to sunset and dusk between approximately 0000-0100 GMT, or 1900-2000 local time).

Sound speed profiles were measured using expendable bathythermograph (XBT) probes at intervals of approximately eight hours during 2011 and six hours during 2012. The sound speed at the depth of the SBES transducer was measured continuously throughout both surveys at a sample rate of 10 Hz and used to convert target electrical phase differences to mechanical angles in the transducer reference frame. Salinity data were derived from conductivity, temperature, and depth (CTD) profiles collected at multiple locations during both cruises. Acoustic absorption profiles were calculated from temperature, salinity, and depth data using the Francois and Garrison model with an estimated pH of 8.0 [21], [22]. All SBES data were processed using sound speed and absorption profiles derived from measurements that were the nearest in time to the acoustic observations.

### **Calibration**

Measurement of the SBES two-way beam pattern for TS calibration was performed during the data collection period in 2011 using a standard SBES calibration method described by [23]. Calibration data were collected by actively transmitting and receiving while maneuvering a standard 60 mm-diameter copper sphere suspended on monofilament line throughout the SBES FOV. Atmospheric and sea conditions were calm and all ship propulsion was secured to reduce water column noise during the TS calibration procedure; additionally, calibration was performed in deep water to reduce reverberation. A theoretical sphere TS of -35.7 dB at 18 kHz was calculated with a software package provided by Dezhang Chu (NOAA NWFSC) using ambient conditions at the sphere depth of 55 m. Temperature of 24.3 °C and salinity of 36.4 ppt at the sphere depth were derived from CTD data collected immediately prior to TS calibration. A piston transducer model [24] was fit to the calibration data, which were collected throughout and beyond the SBES FOV over the angular ranges of -7.3° to +7.2° athwartship and -7.5° to +6.9° alongship.

The resulting piston transducer model yielded the SBES two-way beam pattern and differed from the measured TS calibration data by a mean of +0.2 dB within the -3 dB beamwidth of 12°, enabling calibrated TS calculation for plume targets. Though the Simrad EK60 SBES enables mechanical target angle calculation over a range of 26° in the alongship and athwartship directions, the FOV was limited to the -3 dB beamwidth

of 12° for this study to ensure reliable calculation of TS (i.e., calculation of TS where calibration data existed). Ideally, the TS calibration procedure would have been repeated at the start of data collection in both 2011 and 2012. However, beam pattern corrections derived from 2011 sphere TS data were applied for 2011 and 2012 seep TS measurements because the TS calibration procedure was not repeated before data collection in 2012. No modifications were made to the echosounder between surveys in 2011 and 2012.

### **Positioning and Profiling**

Raw SBES data were parsed with freely available software [25] and manually scrutinized for plume observations, each characterized by a vertically oriented region of elevated scattering strength corresponding with a fore-aft trend in alongship target angle and highly consistent athwartship target angle (Fig. 2). SBES data for pings containing apparent plume targets were isolated for further analysis (Appendix). For each plume, an ambient noise profile was calculated using at least 30 of the nearest pings not containing plume targets. To eliminate bottom returns and weak scatterers from further processing, plume targets were threshold-filtered to exclude those with uncorrected TS outside the range of -40 dB to 0 dB and signal-to-noise ratio (SNR) less than 10 dB.

Corrections for vessel position, vessel attitude, orientation of the SBES transducer in the vessel reference frame, and refraction of the acoustic ray path were applied to georeference threshold-filtered plume targets. These processing routines followed similar methods applied to MBES bathymetric survey data [26], [27]. Uncorrected TS based on the SBES default acoustic absorption rate of 1.5 dB/km at 18 kHz were adjusted for range-dependent cumulative losses based on CTD- and XBT-derived acoustic absorption profiles. The final TS calculation for each georeferenced plume target sample volume was completed by angle-dependent correction based on the SBES two-way beam pattern measured during TS calibration in 2011.

For each plume observation, a gas vent position on the seafloor was estimated by linear least-squares best-fit extrapolation of threshold-filtered and georeferenced midwater target positions in the deepest 200 m to the local mean depth of bottom detection. Linear extrapolation is based on the assumption of

constant and uniform current structure over the path and duration of bubble ascent in this depth range. In addition to estimates of seep source locations on the seafloor, vertical profiles of horizontal plume position (the 'plume axis') and scattering strength were calculated by averaging in vertical bins. A vertical bin width of 100 m was used for the plume axis to reduce apparent noise in the lateral positions of bin centers, assuming that each plume observation corresponds to a discrete stream of bubbles generally rising linearly and vertically with smooth deformations due to current structure [28].

Plume TS profiles were created by averaging the threshold-filtered and georeferenced targets in 20-m vertical bins. The minimum observable plume depth was estimated for each seep by visual scrutiny of scattering strength anomalies and trends in mechanical target angles in the alongship and athwartship directions (Fig. 3). To estimate whether the shallowest vertical extent of each plume observation was limited (or 'cut off') by the SBES beamwidth, the FOV for each ping was calculated using unit vectors that represented all outermost combinations of alongship and athwartship target angles within a mechanical angle of 6° from boresight, or half the -3 dB beamwidth of 12°. These unit vectors corresponded to the outermost target positioning capabilities of the SBES in all directions within the beamwidth-limited FOV. Vectors were transformed for vessel attitude and raytraced using the same sound speed data employed for plume target georeferencing. For each ping, the intersections of raytraced FOV limit vectors with a horizontal plane at the minimum observed plume depth described an approximately circular shape corresponding to the georeferenced outer limits of the echosounder FOV at that depth. The outline of FOV limits for all pings associated with each plume observation was taken as the overall FOV limit at the estimated minimum plume depth. Upper plume positions within the FOV limits indicate the shallowest depths reached by bubbles observable acoustically at 18 kHz without limitation due to transducer orientation. Conversely, upper plume positions on or outside the FOV limits suggest bubbles may have been acoustically observable at shallower depths but were not observed due to reduced sensitivity near or beyond the -3 dB beamwidth of the echosounder. In all cases, acoustic masking of bubbles due to reverberation in the water column or changes in acoustic responses of the bubbles may cause the plume to appear to terminate in acoustic observations at 18 kHz when, in fact, bubbles are still present.



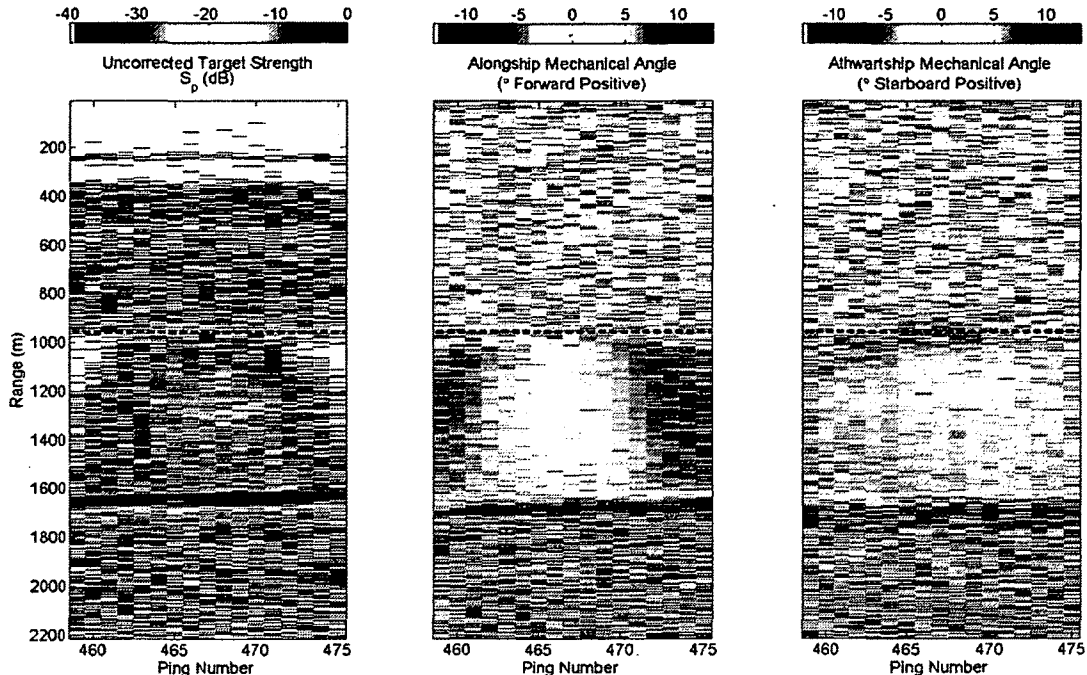


FIGURE 3. Example of minimum plume depth selection (black dashed horizontal line) by visual examination of scattering strength and target angle data. Starting at the seafloor and moving toward the surface, the minimum observable plume height was selected for each seep as the deepest depth at which no scattering strength anomaly and no fore-aft or port-starboard trends in the target angle data remain readily apparent or obviously distinct from the ambient noise data.

### Timing

Variable errors were observed in ping datagram header timestamps due to SBES computer timing drift. SBES ping datagram header timestamps are the only ping timing information in SBES raw data, though the SBES and MBES were synchronized to reduce acoustic interference using a ping trigger provided by the MBES. The variable errors in recorded SBES ping datagram timestamps were sufficiently large to initially cause ambiguity in matching SBES ping times to MBES trigger times. As a first correction, SBES ping datagram header timestamps were adjusted in post-processing by comparison of GPS time data parsed from position datagrams and their respective datagram header timestamps. This step reduced SBES timing errors to approximately 0.1 s and resolved ambiguities in matching SBES ping times to MBES trigger times. As a final correction, SBES ping times were then set to the nearest MBES ping trigger times.

### **Determination of SBES Angular Offsets**

Calibrated TS measurements for unique seep sites required verification of SBES positioning capability for identification of repeat observations of plumes originating from similar locations on the seafloor. Specifically, georeferencing of targets in the SBES echosounder field of view required compensation for the linear and angular offsets of the SBES transducer with respect to the motion sensor reference frame. Linear offsets of the SBES transducer in the motion sensor reference frame were determined by a ship survey after equipment installation and prior to data collection. Angular offsets between the SBES transducer and motion sensor were not surveyed. These angular offsets, if they exist, may lead to range-dependent errors in target positioning and become significantly more important than linear offsets for positioning accuracy in deep water.

To improve SBES seep positioning accuracy, a method was developed to estimate the angular offsets of the SBES transducer with respect to the motion sensor reference frame. This was accomplished by comparison of plume targets in the SBES reference frame to benchmark georeferenced seep positions estimated from simultaneous midwater target data collected in 2011 with a 30-kHz Kongsberg EM302 multibeam echosounder (MBES). MBES systems typically employ many hundreds of narrow beams for high-accuracy swath coverage of the seafloor. MBES systems with midwater mapping capabilities, such as the EM302, may also be used to georeference bubble plumes in the water column. However, MBES systems are typically not employed for midwater TS calculations due to the complexity of field calibration for TS over the large numbers of narrow beams. Accordingly, examination of bubble plumes with SBES is the focus of this thesis, with MBES comparison only for investigation and improvement of SBES positioning accuracy.

For a target near nadir and within the angular range of the SBES FOV, the MBES horizontal positioning uncertainty is estimated from the intersection of a locally flat seafloor with formed beams having -3 dB beamwidths of 0.5° and 1.0° in the alongship and athwartship directions, respectively. Assuming a planar wavefront for the transmit pulse, MBES horizontal positioning uncertainty is approximately 12 m alongship by 24 m athwartship within the -3 dB beamwidths at the survey area depth of 1400 m.

Because the MBES was routinely calibrated for positioning accuracy ('patch tested') [29]–[31] and produced artifact-free bathymetry, gas vent positions estimated from MBES plume observations [28] were treated as benchmarks for SBES gas vent positioning comparison. Ranges of  $-2^\circ$  to  $+2^\circ$  were assigned for initial estimates of roll, pitch, and yaw angular biases of the SBES transducer. For every combination of attitude bias, gas vent positions were estimated for ten SBES plume observations and compared to associated benchmark MBES seep base position estimates. The attitude bias ranges were refined and recentered around the roll, pitch, and yaw combination producing the minimum mean positioning differences from associated benchmarks. Roll, pitch, and yaw bias ranges converged over 20 iterations toward mean values of  $+0.9^\circ$ ,  $-2.1^\circ$ , and  $+5.6^\circ$ , respectively. To reflect the positioning uncertainty inherent in the SBES target angle data, these mean angular bias values were rounded to the maximum achievable mechanical target angle resolution of approximately  $0.1^\circ$  estimated from the rate of electrical phase difference digitization in the SBES raw data. The resulting angular offsets were applied for all SBES plume target positioning and gas vent position estimates.

### Seep Clustering

To identify probable repeat observations of unique gas vent sites across surveys, plume observations were grouped by finding clusters of seep base position estimates in which all seeps were separated by no more than a given 'linking distance' from at least one other seep. The linking distance approximates the largest expected horizontal positioning uncertainty in the survey area according to the split-aperture correlation method employed by the SBES for target angle calculation. Burdic's Eq. 13-103 [32] for a single aperture pair, such as SBES half-arrays in the alongship or athwartship direction individually, leads to the standard deviation of target angle  $\gamma$  for an arriving waveform of wavelength  $\lambda$  measured at acoustic centers with separation  $L$  as

$$\sigma_\gamma = \frac{\lambda}{\pi L} \left( \frac{E[n^2]}{E[s^2]} \right)^{1/2} \quad (1)$$

where  $E[s^2]$  and  $E[n^2]$  are the expected values of the squared signal and noise amplitudes, respectively. Equation 1 is rewritten identifying the quotient of expected values as an estimate of the inverse SNR at the SBES receiver inputs, yielding

$$\sigma_Y = \frac{\lambda}{\pi L \sqrt{d}} \quad (2)$$

where  $d$  is the linear SNR. Equation 2 agrees with Lurton's Eq. 7 [33] for target angles nearly normal to the split-aperture axis, such as those within the SBES beamwidth. As SBES target angle uncertainty increases with reduced SNR, the largest expected target angle standard deviation in the alongship or athwartship direction is estimated from Eq. 2 where  $\lambda = 0.085$  m,  $L = 0.185$  m, and  $d = 10$  for the case of a single plume target with minimum threshold-filtered SNR of 10 dB. The product of target angle standard deviation with the largest target range of approximately 1400 m in the study area yields 65 m as the maximum expected horizontal positioning uncertainty (1 standard deviation) for a single threshold-filtered plume target.

Clustering of seep positions to identify repeat observations of unique gas vent sites across surveys used a linking distance of 65 m to represent the expected maximum positioning uncertainty for repeat observations of seeps. Based on simultaneous 2011 MBES observations, in which plumes near nadir typically subtended angles far less than the SBES beamwidth, gas vents at each seep site were expected to have areal extents much smaller than the SBES beamwidth footprint on the seafloor. Because no seep sites were observed in 2011 with areal extents exceeding the SBES beamwidth footprint (which would be termed 'diffuse' seeps in the view of this echosounder), every SBES plume observation was expected to capture the entire areal extent of the associated seep site on the seafloor. Seep sites of this nature occupy less than the SBES beamwidth-limited ensonified volume and are hereafter described as 'discrete' seeps in this study.

### **TS of Seep Targets**

Midwater gas bubbles of radii much less than the acoustic wavelength scatter incident acoustic energy isotropically by damped harmonic oscillation. The total scattering cross section  $\sigma_s$  for a spherical bubble with radius  $r$  ensonified at frequency  $f$  is given by

$$\sigma_s = \frac{4\pi r^2}{[(f_{res}/f)^2 - 1]^2 + \delta^2} \quad (3)$$

where  $f_{res}$  is the resonance frequency of the bubble under ambient conditions and  $\delta$  is a damping coefficient for thermal and viscous effects depending on the properties of the gas and ambient conditions [19].

For the expected case during data collection of single discrete streams of multiple randomly spaced and non-interacting bubbles in each target sample volume, the collective backscattering strength  $\sigma_{bs}$  is related directly to the number and scattering cross sections of individual bubbles by

$$\sigma_{bs} = \sum_{i=1}^{N_\sigma} N_i \frac{\sigma_{s,i}}{4\pi} \quad (4)$$

where  $N_i$  is the number of bubbles having omnidirectional scattering strength  $\sigma_{s,i}$  at the frequency of ensonification [19] and  $N_\sigma$  is the number of unique omnidirectional scattering strengths present. Target strength TS is thus calculated for a target sample volume containing multiple bubbles as

$$TS = 10 \log_{10} \sigma_{bs} . \quad (5)$$

Figure 4 presents the frequency and radius dependencies of TS for single bubbles of free methane gas. Bubble resonance conditions are characterized by a TS peak for each bubble radius. The radii used in this example are representative of methane gas bubbles observed using remotely operated vehicles (ROVs) equipped with high-definition cameras and visual bubble sizing apparatus during the 2012 data collection period in the vicinity of the study area and by other marine gas investigations in the Gulf of Mexico [34]. Based on the depth and radius dependencies of TS for methane bubbles, changes in TS profiles for processed SBES data represent changes to parameters of the ensonified bubbles acoustically observable at 18 kHz. For instance, changes in TS during bubble ascent may reflect changes in the numbers of bubbles acoustically observable at 18 kHz, changes in the bubble size distribution, changes in the scattering strengths of acoustically observable bubbles, or a combination thereof. Without knowledge of the bubble size distribution in an ensonified target volume, ambiguity exists in the relationship between TS at any single frequency and the total volume of gas ensonified.

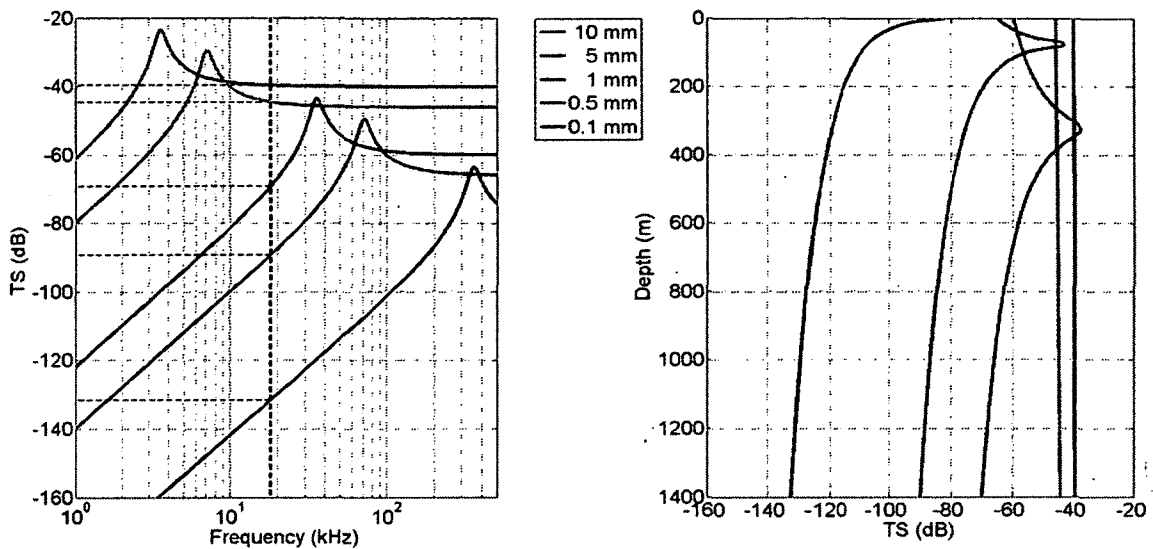


FIGURE 4. Target strength (TS) of free methane gas bubbles. TS peaks indicate bubble resonance. Left: TS versus frequencies of ensonification for a range of bubble radii at depth of 1300 m seawater. Dashed lines indicate the frequency of ensonification during SBES data collection (18 kHz) and corresponding TS. Right: TS profiles for bubbles of several radii ensonified at 18 kHz over the depth range at the survey area.

#### **S<sub>z</sub> for Single Discrete Plumes**

Though gas flux estimation is not possible for bubbles ensonified at a single frequency without knowledge of bubble size distribution, temporal variability in scattering strength may be indicative of relative changes in gas flux for a single source with constant bubble size distribution. Likewise, scattering strength variability along a plume axis in the vertical direction may indicate changes to net vertical gas flux and bubble behavior or survival during ascent. However, TS does not account for the geometry of intersection between the transmit pulse and the plume axis (Fig. 5). This geometry of intersection directly affects the number of bubbles ensonified for a given plume and depends on transmit pulse length, echosounder orientation, and depth-dependent plume deformation due to current structure. Naturally, these parameters vary significantly between seep observations and among echosounder configurations for seep studies.

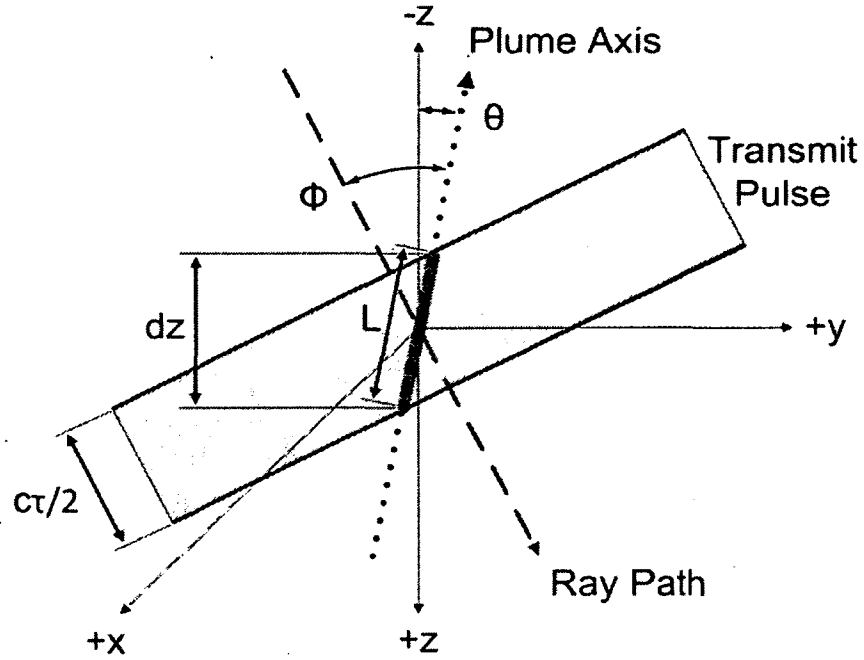


FIGURE 5. Geometry of intersection between the plume axis and transmit pulse contribution to the received signal. The origin coincides with the center of the target sample volume for which TS is calculated. For clarity, azimuth of the plume axis is not indicated. Angular separation  $\Phi$  between the plume axis and ray path vectors lies in the plane containing both vectors.

To account for these variations, a quantity,  $S_z$ , describing TS per unit of vertical dimension of plume ensonification is suggested as

$$S_z = \frac{TS}{dz} \quad (6)$$

where  $dz$  is the vertical extent (m) of plume axis ensonification. From Fig. 5,  $dz$  is calculated as

$$dz = L \cos \theta \quad (7)$$

where  $L$  is the length of intersection between the transmit pulse and the plume axis. Angle  $\theta$  is measured from vertical to the plume axis unit vector,  $\vec{u}_p$ , along which all bubbles are assumed to have the same direction of ascent.  $L$  is calculated as

$$L = \frac{c\tau}{2 \cos \Phi} \quad (8)$$

where  $c$  is sound speed (m/s) at the target estimated from sound speed profile data and  $\tau$  is the transmit pulse length (s).  $\Phi$  is the angle between  $\vec{u}_p$  and  $\vec{u}_r$  calculated from the dot product definition by

$$\cos \Phi = \frac{\vec{u}_r \cdot \vec{u}_p}{|\vec{u}_r| |\vec{u}_p|} \quad (9)$$

where  $\vec{u}_r$  is the unit vector aligned with the refraction-corrected path of the incident planar acoustic wave. For observations of single discrete plumes within the SBES FOV, the quantity  $S_z$  isolates TS from effects of transducer orientation, plume deformation, and changes in pulse length to facilitate comparison of seep scattering strength associated strictly with gas flux in the vertical dimension.

### **Diffuse and Multiple Discrete Plumes**

Characterization of relative gas flux by  $S_z$  is appropriate for single discrete plumes observed within the SBES FOV, as the collective backscattering strength for a single stream of bubbles in each target sample volume is expected to be the only significant contributor to TS for each target range. Because beam pattern compensation for TS calculation depends on accurate target angle calculation, which is confounded by the presence of strong scatterers at different target angles at each range, cases of multiple discrete plumes within the SBES FOV are likely plagued by erroneous target positioning, TS correction, and  $S_z$  calculation. The water column mapping software FMMidwater was used to establish the number of plumes distinguishable in the 2011 MBES data for each SBES observation. Cases of multiple discrete plumes within the SBES FOV were excluded from further TS and  $S_z$  analysis.

Diffuse plumes occupying volumes greater than the beamwidth-limited FOV may not be characterized by  $S_z$  for similar reasons. In these cases, volume scattering strength ( $S_v$ ) is a more appropriate measure of collective scattering strength for randomly spaced, non-interacting bubbles [19]. Based on limited visual investigation with ROVs during survey operations in 2012, the lateral extents of gas vent sites considered here are assumed to fall within the beamwidth footprint on the seafloor and, accordingly, the SBES plume observations are characterized by  $S_z$ .



## CHAPTER II

### RESULTS

#### **Seep Observations and Positions**

To identify repeat observations of unique seeps at similar locations throughout the study area, gas vent position estimates calculated from SBES plume data were grouped (or 'clustered') using a linking distance of 65 m. This method yielded 35 clusters, each including between 1 and 25 SBES observations on repeat survey lines, with a total of 161 seep position estimates among all clusters (Fig. 1, Table 2). For each cluster, the mean of SBES gas vent position estimates was taken as the cluster center (Table 2). Nine clusters contained SBES observations from both 2011 and 2012, whereas eight clusters contained only 2011 data and eighteen clusters contained only 2012 data. These differences in plume counts per cluster between years are related primarily to realignment of the survey trackline from 2011 to 2012. Among clusters containing two or more plume observations, the horizontal differences between estimated gas vent positions and cluster centers on the seafloor averaged 35 m with a standard deviation of 19 m.

To examine the SBES seep positioning accuracy, SBES gas vent position estimates were compared to 'benchmark' positions from simultaneous MBES observations [12] in 2011 (Fig. 6). As described for determination of SBES angular offsets, the MBES horizontal positioning uncertainties for seeps observed within the SBES FOV are approximately 12 m alongship and 24 m athwartship within the -3 dB beamwidths at 1400 m depth.

TABLE 2. Cluster identification number, position, seafloor depth, and number of seep observations. Easting, northing, and depth are meters in UTM zone 16 North, WGS84.

Number	Easting	Northing	Depth	Seep
1	354303	3175414	1380	1
2	354496	3175334	1378	1
3	354580	3175346	1381	1
4	354377	3175132	1375	13
5	354481	3175165	1383	1
6	354580	3174873	1390	1
7	354500	3174813	1382	9
8	354829	3174290	1386	4
9	354936	3174308	1383	1
10	355336	3173712	1358	1
11	355382	3173621	1357	10
12	355454	3173350	1361	1
13	355398	3173251	1354	1
14	355528	3173268	1362	1
15	355595	3173174	1364	1
16	355562	3173100	1362	5
17	355525	3173022	1358	1
18	355672	3173076	1366	1
19	355747	3173004	1365	11
20	355997	3173041	1367	1
21	355945	3172735	1375	1
22	356013	3172612	1374	13
23	355937	3172462	1378	1
24	356010	3172441	1375	1
25	356225	3172265	1380	5
26	356112	3172151	1377	4
27	356725	3171248	1408	19
28	356807	3171220	1409	2
29	356649	3171040	1418	1
30	356913	3171111	1417	2
31	357000	3170877	1420	1
32	356914	3170695	1407	1
33	357018	3170744	1420	25
34	357579	3169700	1417	15
35	357849	3169590	1412	4

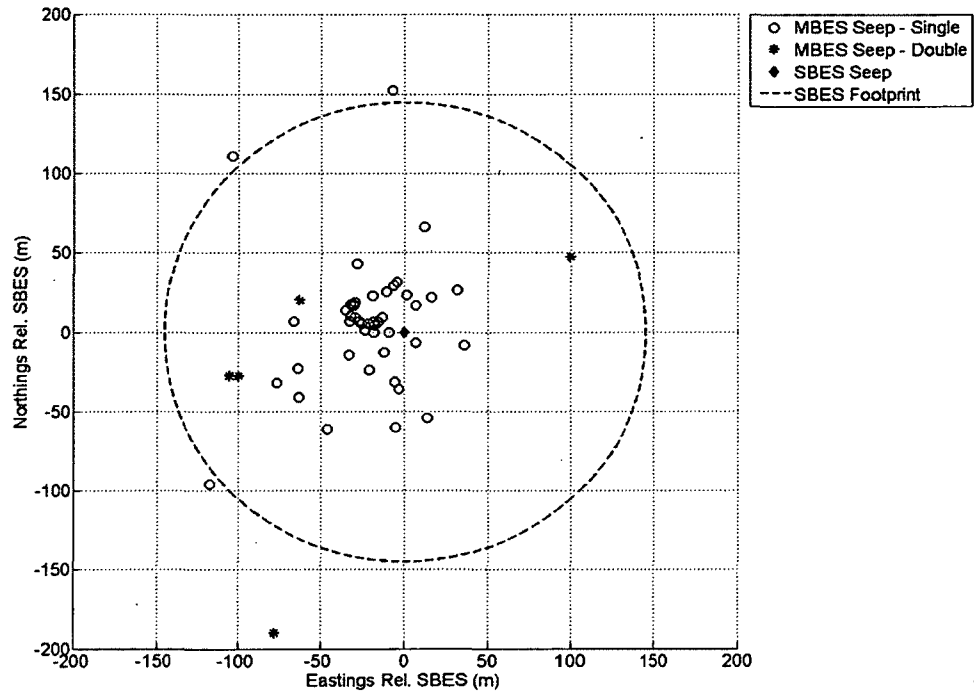


FIGURE 6. Relative MBES (circles) and SBES (diamond, origin) gas vent position estimates for single, distinct plumes observed in 2011. On three occasions, single SBES plume observations were determined to each include two plumes distinguishable in the MBES data (asterisks), for a total of six distinct MBES plume observations among these cases. Only five asterisks are shown because one of the six distinct MBES observation was insufficient for positioning. The SBES beamwidth footprint of 145 m radius at 1400 m depth (dashed line) is centered at the origin for reference only and does not represent SBES FOV coverage relative to SBES or MBES gas vent position estimates.

Seven of the 55 SBES plume observations in 2011 were obscured by noise in the MBES data and were not used for positioning comparison. Differences between concurrently observed SBES and MBES gas vent position estimates had a mean of 51 m and standard deviation of 42 m for the 48 SBES observations in 2011 for which MBES data were available. Of these 48 SBES observations, 45 were determined to contain single discrete plumes and three were determined to each contain two discrete plumes distinguishable in the MBES data. The positioning difference mean and standard deviation are reduced to 44 m and 34 m, respectively, for the 45 cases of single discrete plume observations. Three of these 45 SBES seep base position estimates fall beyond the SBES footprint radius from the MBES benchmark and may be considered outliers of the seep processing method. Removing these from comparison further reduces the SBES and MBES positioning difference mean and standard deviation to 36 m and 19 m, respectively, for the 42 MBES

benchmarks falling within the SBES footprint radius of 145 m. These results suggest SBES seep positioning accuracy on the order of MBES positioning capability for most cases of single discrete plumes. Given the predominantly NNW survey heading for these seep observations, the mean difference and ship-relative bearing to seep base estimates also indicate bias in SBES seep base positioning relative to the MBES benchmarks (Fig. 6). The mean position of SBES gas vent estimates is 36 m at a vessel-relative bearing of 123° compared to the mean of MBES benchmarks within the SBES footprint radius. These mean range and bearing values correspond to alongship and athwartship SBES position biases of 20 m astern and 30 m to starboard, respectively. At 1400 m depth in the survey area, these mean directional differences between SBES gas vent position estimates and MBES benchmarks suggest unresolved SBES angular biases of 0.8° alongship and 1.2° athwartship.

#### **S<sub>z</sub> Profiles and Plume Depths**

Profiles of S<sub>z</sub> versus depth were created for all plume observations, examples of which are shown in Fig. 7 for 2011 and 2012 plume observations at cluster 22. Noise profiles based on TS uncorrected for SBES beam pattern appear as dashed lines and show the effects of threshold filtering for SNR on behavior of S<sub>z</sub> profiles, which sometimes follow the slope of the associated ambient noise profile.

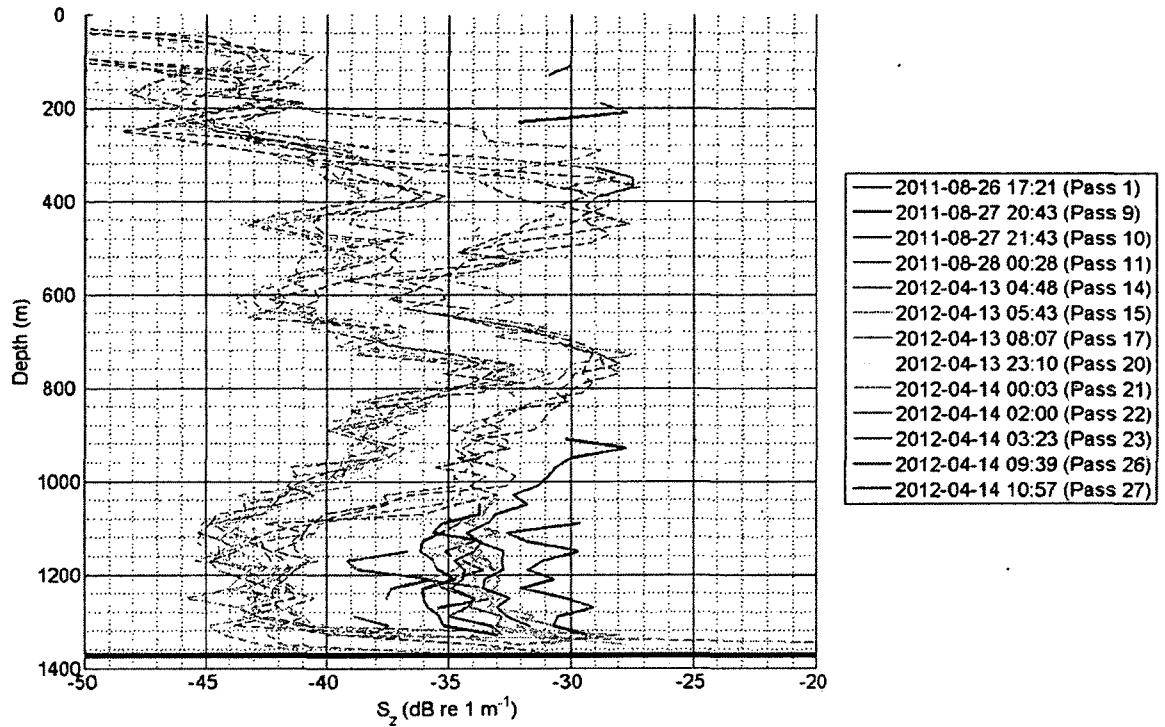


FIGURE 7. Examples of  $S_2$  profiles (solid lines) and ambient noise profiles (TS uncorrected for beam pattern, dashed lines) for repeat plume observations at cluster 22. Colors correspond to survey pass number and time of observation. The horizontal red line represents the mean depth of bottom detection. Most profiles terminate below approximately 1000 m, likely as a consequence of threshold filtering for  $\text{SNR} \geq 10$  dB in the vicinity of increased noise associated with the deep scattering layer (DSL) between 600-900 m. Filtered targets are observed on at least two occasions above the DSL, though these shallowest targets are disconnected from the deeper profile sections by more than 500 m and are not assumed to represent the minimum plume depths.

The minimum acoustically observable plume depth was estimated for every plume observation by visual scrutiny of TS and target angle data (e.g., Fig. 3), yielding minimum plume depth estimates with a mean of 875 m. The shallowest observed plume depth was approximately 360 m, with 32 plumes (20% of all observations) rising to depths shallower than 600 m (Fig. 8). Most profiles were observed to terminate below 600-800 m, one of several depth ranges characterized by increased densities of biological acoustic scatterers known collectively as the 'deep scattering layer (DSL)' [35] (Figs. 2, 3, and 7). For example, two distinct depth ranges within the DSL are visible in the top panel of Fig. 2, with two plume observations appearing to terminate in the deeper layer between 800-1200 m depth.

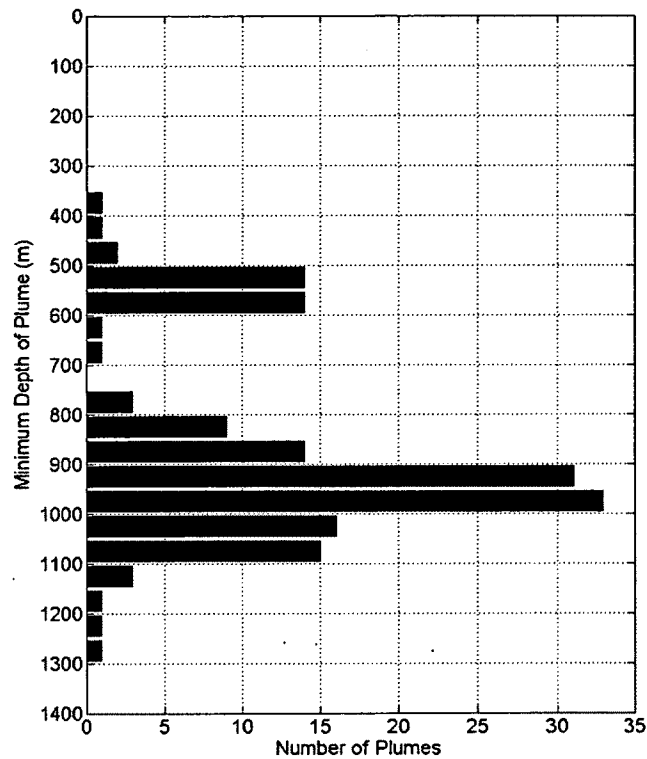


FIGURE 8. Distribution of minimum plume depths observed acoustically at 18 kHz based on manual scrutiny of TS (uncorrected for SBES beam pattern) and trends in alongship and athwartship mechanical angles. Of 161 plumes originating at approximately 1400 m depth in the seep study area, 156 appeared to terminate within the echosounder FOV. Minimum depth estimates fell outside the echosounder FOV on five occasions and were likely limited (or 'cut off') by the echosounder FOV. Four of these five minimum observed plume depths fell between 1000-1200 m and one was estimated at approximately 550 m.

In general, the DSL between 600-900 m depth tended to divide the observations of minimum plume height into a bimodal distribution, with 34 plumes (21% of all observations) appearing to reach depths shallower than 700 m and the remainder terminating below 750 m (Fig. 8) with no estimates between 700-750 m; this dividing effect of the DSL contributes to the relatively large standard deviation of 191 m among all minimum observed plume depths. Limitations of the SBES FOV did not appear to impact a significant portion of minimum plume depth estimates. Of 161 plume observations, 156 (97%) were observed to terminate within the SBES FOV and 5 were likely 'cut off' by the FOV. Four of the five FOV-limited minimum plume depth estimates fell within the depth range of 1020 - 1200 m, with one estimate at 550 m.

Mean  $S_z$  values in the deepest 200 m were calculated from  $S_z$  profiles for comparison of temporal changes to seep activity at the gas vent sites, including apparent starting and stopping of gas flow of bubbles acoustically observable at 18 kHz (Fig. 9). The depth range of 200 m was selected to include targets in the ten deepest  $S_z$  profile depth bins, each of which has a width of 20 m. Mean  $S_z$  values in the deepest 200 m were calculated for all but one observation, at which the  $S_z$  profile contained insufficient data for averaging in the deepest 200 m ('X', Fig. 9). In one case, two separate SBES seep observations during one survey pass satisfied the seep clustering proximity criterion and were assigned to a unique cluster; Fig. 9 includes both mean  $S_z$  values in the deepest 200 m as a diagonally split cell. Coverage for the echosounder FOV on the seafloor was estimated for each survey pass to determine whether a plume at each cluster position would have fallen inside or outside the horizontal range of plume positions expected to be visible. In cases of no plume observation within a cluster during a survey pass, an indication is made in Fig. 9 for whether the cluster position fell within the echosounder FOV on the seafloor and was expected to be visible. Means of plotted values for each cluster across all passes and each pass across all clusters are plotted on the right side and bottom of Fig. 9, respectively.

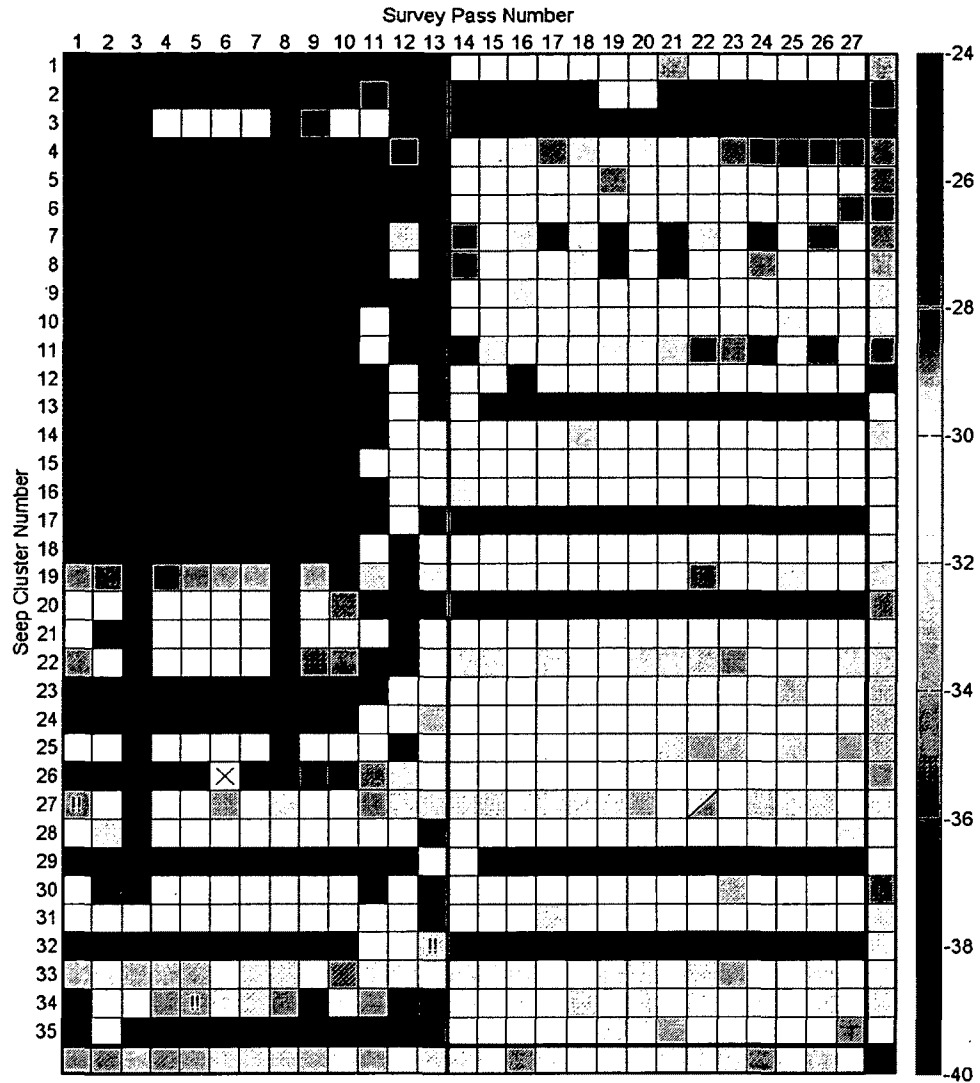


FIGURE 9. Mean  $S_2$  in the deepest 200 m for all seep observations at each cluster during all survey passes. White indicates that the cluster position was expected to pass within the echosounder field of view but no plume was observed; black indicates passes during which the cluster position was not expected to be visible due to ship position and orientation of the echosounder field of view. In one instance, two separate seep observations on a single survey pass (22) satisfied the cluster linking distance criterion and were associated with the same cluster (27); these observations are represented by a split cell with the upper and lower triangle colors pertaining to the first and second seep observations, respectively. The 'X' for cluster 26 during pass 6 indicates that a seep was observed but the  $S_2$  profile contained insufficient data for calculation of mean  $S_2$  in the deepest 200 m. For the 55 SBES plume observations in 2011, MBES data suggest that two distinct plumes are included within the SBES FOV on three occasions; these instances are marked by double exclamation points. 2012 MBES data have not been reviewed for similar instances. Means of the plotted values for each cluster and each survey pass are shown in the right column and bottom row, respectively.



## CHAPTER III

### DISCUSSION

#### **Seep Positioning and Clustering**

For individual gas vents separated by more than the SBES beamwidth footprint on the seafloor, the development and application of processing steps for georeferencing plume targets observed with the SBES has been shown to yield seep positioning accuracy commensurate with that of the MBES calibrated for bathymetric and midwater mapping used in this study. These results suggest that plumes detected with SBES and traced to similar seafloor positions correspond to repeat observations of unique gas vent sites within the positioning resolution of the SBES and facilitate comparison of scattering strength profiles based on repeat measurements of calibrated TS for plumes originating at unique gas vent sites on the seafloor. Likewise, barring other factors which may inhibit the detection of plumes, the SBES positioning capability demonstrated here increases confidence in the conclusions of absence of bubbles acoustically observable at 18 kHz when the echosounder FOV includes a known gas vent site (or cluster of gas vent sites) but no plume is observed.

Though seeps were observed repeatedly during survey passes conducted on two narrow ranges of headings (NNW and SSE), MBES gas vent position benchmarks are distributed among all quadrants relative to simultaneous SBES position estimates and typically differ by an order of magnitude less than the SBES footprint. These results suggests that the erroneous SBES timing data and unknown SBES transducer angular offsets, the most likely contributors to large and systemic positioning errors, have been substantially resolved. Timing correction and angular offset estimation appear to be practical and worthwhile steps for georeferencing SBES data in future studies.

The disadvantages of seep positioning with SBES are related to beamwidth and availability of target angle data within the beamwidth-limited FOV. Of primary consequence, the SBES beamwidth of 12° provided limited athwartship FOV coverage compared to MBES. Second, the ability to distinguish among separate plumes rising simultaneously within the FOV is limited by the SBES split-aperture correlation method, which produced one pair of alongship and athwartship target angles per range sample per transmit-receive cycle. This second concern may be addressed in future studies by closer examination of target angle data which cannot be readily distinguished visually. For instance, data selected for a plume observation may contain threshold-filtered targets associated with multiple plumes originating from more than one discrete gas source on the seafloor. In this case, separate fore-aft trends in alongship target angle that are correlated with distinct and consistent athwartship target angles may indicate discrete plumes detected within the beamwidth. No attempt was made in this study to distinguish among target angle trends within each selected plume observation. All threshold-filtered targets within each SBES plume observation were attributed to a single seep location, limiting the distinction of discrete gas vents falling within the SBES beamwidth and requiring scrutiny of MBES data to identify instances of multiple plumes. MBES data from 2011 showed two distinct plumes for 3 out of the 55 concurrent SBES plume observations, suggesting that the assumption of single seep contributions to SBES TS data and target angle measurements is applicable to the large majority of plume observations.

Plume observations were clustered for evaluation of temporal variability based on the proximities of their estimated gas vent positions to each other within the SBES horizontal positioning uncertainty of 65 m for a single plume target passing the minimum SNR threshold filter. The resulting cluster locations were typically separated by at least several hundred meters (Fig. 1) and seep positions in each cluster typically spanned no more than the SBES beamwidth footprint on the seafloor. As expected for clusters of distinct gas vent sites, a maximum one plume observation per survey pass was made at each cluster during almost all passes. On only one occasion, two unique plumes and their associated distinct seep position estimates observed on a single pass were later assigned to the same cluster. This 'dual-seep' observation was recognized as an artifact of the clustering method, which otherwise succeeded in identifying and assigning

a maximum of one seep observation per pass to each cluster based on proximity alone. It is important to note that cluster boundaries had no typical shape, as the linking distance had no directional component and was applied with the sole intent of grouping seep base position estimates by proximity. The absence of any general trends in cluster shapes suggests that seep locations were not consistently distributed within each cluster. This distribution of seep positions within a cluster may be a result of random measurement error, movement of the seabed source of bubbles, or a combination of these factors.

Though identified and isolated as distinct clusters by the linking distance of 65 m, several of the 20 clusters containing only one seep lend themselves to consideration alongside other nearby clusters that also contained one or more seeps. This is evident primarily where the clustering process has produced multi-seep clusters that are extended in the alongtrack direction but excluded nearby isolated seeps that did not meet the linking distance criterion. For example, single-seep cluster 5 falls within the alongtrack extent of multi-seep cluster 4, which itself has a distribution of seep positions roughly equal to the separation between clusters 4 and 5 (approximately 120 m, or less than the SBES beamwidth footprint radius at 1400 m). The single seep observation in cluster 5 was made during pass 19, corresponding with a plume absence in cluster 4 and raising the possibility that plume observations in clusters 4 and 5 are related and may originate from the same near-surface network of gas venting pathways. Similar consideration may be applied for the pairs of single-seep clusters 6 and 9 with multi-seep clusters 7 and 8, respectively. There are also instances of closely spaced but distinctly numbered multi-seep clusters containing plume observations which may be related. For example, cluster 27 contains 19 seeps which satisfy the linking distance criterion but are spread alongtrack over approximately 250 m. This alongtrack distance overlaps that of cluster 28, which is centered less than 100 m from the center of cluster 27 and includes two seeps observed on passes with no observations at cluster 27. Though these clusters were identified and separated based on proximity of individual seep observations, the spacing and timing of those observations suggest that seeps in clusters 27 and 28 are closely related. These examples raise the possibility that the simple linking distance clustering method may not adequately capture temporal relationships between nearby seep sites and may yield cluster dimensions much larger than the beamwidth footprint. Additional

consideration for the timing of seep observations in close proximity during the clustering process may prove useful in grouping vent sites which exhibit related gas flow even if physically separated by more than the linking distance. Likewise, timing criteria would aid in delineating among seeps which satisfy a given linking distance but are not related in their flow behaviors. In this study, the linking distance of 65 m was applied as a simple grouping criterion and generally produced well-separated clusters containing one repeat seep observation per pass. This method could be readily applied to future seep studies, with adjustment of the linking distance appropriate for the echosounder beamwidth.

### **Plume Observations and S<sub>z</sub> Profiles**

The SBES FOV coverage of clusters 1, 4-12, 14-16, 18, 23-24, 26, and 35 was limited during 2011 due to alignment of the survey trackline, which was adjusted by approximately 5° in 2012 to provide more consistent coverage of all clusters (Fig. 1). Clusters 2-3, 13, 17, 29, and 32 included only single seep observations in locations that fell just beyond the FOV coverage for most passes during both surveys; as such, coverage did not improve at these clusters from 2011 to 2012. Despite the survey trackline realignment and associated change in FOV coverage, no appreciable difference was noted between 2011 and 2012 in the variability of plume observation rates. For instance, the ratio of total plume observations to number of cluster locations visited varied from low ratios of 3:12 [0.25] during passes 5 and 7 in 2011 and 5:27 [0.19] during pass 17 in 2012 to highs of 3:6 [0.50] and 6:12 [0.50] during passes 8 and 9 in 2011 and 10:28 [0.36] in passes 22 in 2012. Per-pass rates of plume observation in 2011 and 2012 averaged 0.35 and 0.27, respectively. These results suggest that an average of approximately one-third of seep locations in this study were observed to be venting gas during any given survey pass and that there was no appreciable change in plume presence across the entire survey area during the 2011 and 2012 data collection periods.

Though a general trend in seep activity is not evident for the entire survey area, individual clusters varied widely in the rates of plume observations across all passes within the FOV. These rates ranged from lows of 1:26 [0.04] at cluster 31 and 1:23 [0.04] at cluster 21 to a high of 25:27 [0.93] at cluster 33, with each

cluster typically falling within the SBES FOV during 2011 and 2012. Average plume observation rates at each cluster, accounting for FOV coverage for all passes, resembled per-pass rates across all clusters with a mean of 0.31; the standard deviation of 0.29 in per-cluster plume observation rate reflects the wide variability in total plume observations at each cluster location across surveys. Importantly, there was no single cluster that was observed on every survey pass, nor was there any single survey pass which observed plumes at all of the cluster locations. Conversely, no survey pass included zero plume observations. Taken together, these results suggest that the rates of plume observations at clusters falling within the SBES FOV are indicators of plume presence or absence which are independent of survey trackline orientation and dependent primarily on behaviors of the individual seep sites.

$S_z$  profiles for plumes observed at cluster 22 (e.g., Fig. 7) show that upper plume observations were significantly limited by reverberation in the DSL. This shallow limit applied to most plume observations, as evidenced by the sharply decreasing frequency of minimum plume depths in the depth range of 600-900 m (Fig. 8). Approximately 80% of all plumes were observed to terminate deeper than 600 m. The widespread and consistent reduction of bubbles detectable at 18 kHz at depths shallower than 600 m likely correspond with reduction in bubble size due to gas transfer out of the bubbles during ascent [36], [37].

For 32 plume observations, gas transfer out of the bubbles was sufficiently slow to enable survival of bubbles detectable at 18 kHz to depths shallower than 600 m. In one case, a plume reached as shallow as 360 m, though no plume observations extended shallower than this depth. Only one plume observation reaching a depth shallower than 600 m was limited by the echosounder FOV (at approximately 550 m), suggesting that bubbles which had been consistently acoustically observable at 18 kHz during the 800-m ascent from the seafloor to a depth of 600 m dissipated rapidly over the subsequent 250 m. These observations suggest enhanced survival of bubbles for a small number of plumes, followed by rapid reduction of detectable bubbles at depths shallower than 600 m. Formation of methane hydrate shells on the bubbles has been suggested as a mechanism which may inhibit gas transfer and increase the duration of bubble survival for methane bubbles originating at the depth of the survey area and ascending through the depth range over which methane hydrates are stable [3], [14], [34], [36]–[38]. The shallow depth limit

of the hydrate stability zone (HSZ), beyond which hydrates will dissociate at shallower depths, typically falls between 500-600 m in the Gulf of Mexico [12], [39], [40]. This shallow limit of the HSZ coincides with the depth range containing most of the shallowest depths of detectable bubble survival during this study, suggesting rapid dissolution of methane gas bubbles after dissociation of their hydrate shells. The acoustic effects of methane hydrate shells on TS for bubbles are areas of active research and were not considered here, apart from this discussion of shallow plume observations related to the reduced dissolution of acoustically observable bubbles during ascent through the HSZ.

### **S<sub>z</sub> Base Variability**

As shown in Fig. 9, a wide range of mean S<sub>z</sub> in the deepest 200 m was observed throughout the 2011 and 2012 surveys. Assuming constant distributions of bubble sizes at each cluster, fluctuations in mean S<sub>z</sub> of +/-3 dB re 1 m<sup>-1</sup> would correspond to doubling or halving, respectively, the numbers of bubbles per vertical meter. In general, mean S<sub>z</sub> values for clusters on the NNW end of the survey line (e.g., clusters 1-9) appear consistently 2-4 dB re 1 m<sup>-1</sup> higher than those for clusters closer to the middle of the survey line (e.g., clusters 10-26). Survey pass 12 includes the only 2011 plume observations on the NNW end of the survey line at clusters which were also observed with seeps in 2012; these clusters (4 and 7) shows relatively consistent agreement in mean S<sub>z</sub> between surveys in 2011 and 2012.

A greater number of plumes were observed during NNW-heading passes than SSE-heading passes in 2012. This pattern is most obvious in seep detections at cluster 34 (Fig. 9), for which plume presence is directly correlated with ship heading in 2012. The unlikelihood of a correlation between gas flow at a cluster and ship heading suggests a difference between estimated FOV coverage and the practical limits of plume target detection during SBES data processing and threshold filtering. Cluster 34 was investigated as a primary example of possible 'false positive FOV coverage' estimates in 2012 (Fig. 9, cluster 34, odd-numbered passes 15-27). To investigate FOV coverage at cluster 34, the closest approach of the ship to the cluster center during each pass was calculated for comparison to the FOV footprint on the seafloor. The athwartship FOV coverage differs to port and to starboard due to transducer roll offset and vessel roll,

which is affected primarily by vessel loading, wind, and sea state. Except for three passes in 2011 (black boxes, Fig. 9), the ship passed within 100 m athwartship of cluster 34 on all passes in 2011 and 2012. These athwartship pass distances fell well within the expected FOV coverage of 160 m to port, the bearing to cluster 34 during NNW-heading survey passes in 2012. This is in agreement with plume observation patterns in this data collection period. During SSE-heading passes in 2012, FOV coverage to starboard was reduced to approximately 100 m by a combination of transducer roll offset and vessel roll. Closer comparison of the cluster position relative to FOV coverage during these SSE-heading passes showed that cluster 14 typically fell within 30 m of the limit of the expected FOV coverage, or approximately 1° of the -3 dB beamwidth.

The FOV was defined in this study by the -3 dB beamwidth of the SBES, and every plume observation included threshold-filtered targets within this angular range. Plume targets were also frequently detected at angles outside the -3 dB beamwidth. These targets were not included in TS calculations due to limited beam pattern correction data beyond the -3 dB beamwidth, but suggest capability for plume detection outside the beamwidth-limited FOV coverage estimate. One related concern would be detection of plumes with targets exclusively outside the -3 dB beamwidth. In this case, a plume would have been detected but not represented in the seep position estimates or TS calculations. However, the careful visual scrutiny of the TS data echograms (similar to Figs. 2 and 3) during plume selection and subsequent confirmation that all plume observations included targets inside the -3 dB beamwidth suggest that the physical presence and absence of plumes during survey passes are faithfully represented in the positioning and TS results.

Periods of consistent plume presence or absence were noted to change for several clusters between 2011 and 2012. For example, a plume was observed at cluster 19 during all survey passes within the FOV in 2011 but only two passes (on both NNW and SSE headings) in 2012. The practical athwartship limit for plume detection at this cluster was not expected to be a factor in this observed change, as the two observations in 2012 were made on different headings and cluster 19 fell well within the FOV coverage estimate for all passes. Similarly, no plumes were observed at cluster 25 in 2011 but were frequently observed starting with pass 21 in 2012. These patterns suggest that gas flow at several clusters switches

between 'on' and 'off' with time scales varying within and between each survey. Among consecutive plume observations at individual clusters with consistently detectable gas flow, the mean  $S_z$  values in the deepest 200 m appear to remain generally within  $\pm 1$  dB re  $1 \text{ m}^{-1}$  from pass to pass over time scales of 1 hour to 7 months (e.g., Fig. 9, cluster 4, passes 22-27; cluster 27, passes 12-18). Less frequently, larger  $S_z$  variations up to 10 dB re  $1 \text{ m}^{-1}$  were observed between subsequent passes separated by less than 2 hours (e.g., Fig. 9, cluster 11, passes 22-24). These observations suggest a high degree in variability of active gas flow at the seep study sites across all surveys.

At several locations along the survey lines there are groups of consecutively numbered clusters falling within a beamwidth footprint on the seafloor of each other, from which a maximum of one plume is observed per group per survey pass. These groups include clusters (4 and 5), (6 and 7), (8 and 9), (10 and 11), (21 through 24), (27 and 28), and (31 through 33). The general pattern of plume observations at only one cluster in each group per survey pass suggests possible connections in gas flow between the separately clustered seep sites in each group, by which gas tends to flow at only one of the clusters within each group at any given time. Likewise, instances of no plume observation during a pass over each group may be associated with gas flow at nearby gas vent sites outside the FOV coverage, though this cannot be shown without additional survey data.



## CHAPTER IV

### CONCLUSIONS

A method for bubble plume detection and positioning has been demonstrated with a split-beam scientific echosounder (SBES) employed for repeat surveys over a region of natural methane seeps at approximately 1400 m depth in the northern Gulf of Mexico. Georeferenced positions of seeps observed repeatedly were identified in 35 clusters, 15 of which included more than one seep observation. Gas vent position estimates in the 15 multi-seep clusters typically fell within 35 m of the cluster centers, distributed over an area substantially smaller than the SBES beamwidth footprint of 290 m diameter. Seep positions were compared to those detected and georeferenced with a multibeam echosounder (MBES) used for simultaneous midwater mapping in 2011, with the distributions of both SBES and MBES seep locations suggesting similar seep positioning accuracy for discrete gas vents on the seafloor.

The limits of the SBES field of view (FOV) were incorporated into survey coverage estimates to determine the visibility of each cluster during repeat survey lines; these limits were also used to establish whether observations of the shallowest portions of plumes were 'cut off' by the echosounder beam pattern and orientation. Despite changes to the survey trackline between data collection periods, the average rates of plume observations across cluster sites visited remained steady at approximately 1/3 in 2011 and 2012. Based on careful visual scrutiny of the raw SBES data, the inclusion of threshold-filtered targets within the -3 dB beamwidth for all plume observations, and the ability to detect plume targets beyond the -3 dB beamwidth, the physical presence and absence of plumes during the surveys are believed to be accurately reflected in the plume observation results.

The shallowest portions of plumes detectable at 18 kHz fell well within the SBES FOV for 97% of plume observations, suggesting that the SBES beamwidth did not significantly limit estimates of minimum plume

depths. Approximately 80% of plumes were observed to terminate deeper than 750 m, routinely within the deep scattering layer (DSL) where scattering from biological organisms may have masked the acoustic returns from gas bubbles. Only 20% of plumes were observed to pass through the DSL and reach depths of 600 m or shallower, of which none were detected shallower than 360 m. In these cases, the survival of bubbles detectable at 18 kHz during the 800-m ascent from 1400 m to 600 m depth is followed by extinction during the much shorter (maximum 240-m) ascent from 600 m to a minimum depth of 360 m. These observations suggest inhibition of gas transfer by methane hydrate coatings on bubbles deeper than the shallow limit of the hydrate stability zone (HSZ) at approximately 600 m.

SBES systems for which *in situ* beam pattern corrections have been determined offer a significant advantage over other echosounders, facilitating calibrated TS measurements for volumes of bubbles rising from natural methane seeps at 1400 m water depth in this study. Though gas flux cannot be established from TS measurements at a single frequency without knowledge of the bubble size distribution, a unit  $S_z$  equal to the TS normalized for the vertical extent of plume axis ensonification was employed to facilitate relative comparison of gas flux under the assumption of constant bubble size distribution (substantiated by ground-truth observations).  $S_z$  represents TS isolated from the effects of changes in transmit pulse length and geometric orientation between the echosounder and plume axes. Under the assumption of constant bubble size distribution, relative magnitudes of gas flux within the survey area were observed to fluctuate widely, with  $S_z$  varying over -39 to -24 dB re  $1 \text{ m}^{-1}$  among all seep observations across all surveys. Smaller variations of  $\pm 1 \text{ dB re } 1 \text{ m}^{-1}$  were typical for plume observations at active seep sites between successive survey passes conducted at time intervals of 1 hour to 1 day. Plume behavior across all clusters was observed to vary from apparently steady gas flow or steady plume absence at some clusters during each data collection period to multiple apparent starts and stops in gas flow on time scales of hours. These results in georeferencing gas vent locations, establishing plume presence and absence, and collecting calibrated TS data to inform  $S_z$  calculation collectively demonstrate the suitability of SBES for seep mapping and monitoring. With knowledge of bubble size distribution,  $S_z$  data offer a step toward standardized gas flux calculation across seep investigations and echosounder configurations.

## LIST OF REFERENCES

- [1] M. Hovland, S. Jensen, and C. Fichler, "Methane and minor oil macro-seep systems - their complexity and environmental significance," *Mar. Geol.*, vol. 332–334, pp. 163–173, Dec. 2012.
- [2] E. A. Solomon, M. Kastner, I. R. MacDonald, and I. Leifer, "Considerable methane fluxes to the atmosphere from hydrocarbon seeps in the Gulf of Mexico," *Nat. Geosci.*, vol. 2, no. 8, pp. 561–565, Jul. 2009.
- [3] A. G. Judd, "Natural seabed gas seeps as sources of atmospheric methane," *Environ. Geol.*, vol. 46, no. 8, pp. 988–996, Jun. 2004.
- [4] A. G. Judd, "The global importance and context of methane escape from the seabed," *Geo-Marine Lett.*, vol. 23, no. 3–4, pp. 147–154, Dec. 2003.
- [5] J. Greinert and B. Nützel, "Hydroacoustic experiments to establish a method for the determination of methane bubble fluxes at cold seeps," *Geo-Marine Lett.*, vol. 24, no. 2, pp. 75–85, May 2004.
- [6] J. Mienert, "Signs of instability," *Nature*, vol. 490, no. 25 October 2012, pp. 491–492, 2012.
- [7] A. G. Judd, M. Hovland, L. I. Dimitrov, S. Garcia Gil, and V. Jukes, "The geological methane budget at Continental Margins and its influence on climate change," *Geofluids*, no. 2, pp. 109–126, 2002.
- [8] L. Naudts, J. Greinert, Y. Artemov, P. Staelens, J. Poort, P. Van Rensbergen, and M. De Batist, "Geological and morphological setting of 2778 methane seeps in the Dnepr paleo-delta, northwestern Black Sea," *Mar. Geol.*, vol. 227, no. 3–4, pp. 177–199, Mar. 2006.
- [9] J. Greinert, "Monitoring temporal variability of bubble release at seeps: the hydroacoustic swath system GasQuant," *J. Geophys. Res.*, vol. 113, no. C7, p. C07048, Jul. 2008.
- [10] Y. G. Artemov, "Software support for investigation of natural methane seeps by hydroacoustic method," *Mar. Ecol. J.*, vol. 5, pp. 57–71, 2006.
- [11] J. S. Hornafius, D. Quigley, and B. P. Luyendyk, "The world's most spectacular marine hydrocarbon seeps (Coal Oil Point, Santa Barbara Channel, California): quantification of emissions," *J. Geophys. Res.*, vol. 104, no. C9, pp. 20703–20711, 1999.
- [12] T. C. Weber, L. Mayer, J. Beaudoin, K. Jerram, M. Malik, B. Shedd, and G. Rice, "Mapping gas seeps with the deepwater multibeam echosounder on Okeanos Explorer," *Oceanography*, vol. 25, no. 1, Supplement, pp. 54–55, 2012.
- [13] A. T. Jones, J. Greinert, D. A. Bowden, I. Klaucke, C. J. Petersen, G. L. Netzeband, and W. Weinrebe, "Acoustic and visual characterisation of methane-rich seabed seeps at Omakere Ridge on the Hikurangi Margin, New Zealand," *Mar. Geol.*, vol. 272, no. 1–4, pp. 154–169, Jul. 2010.
- [14] J. Greinert, Y. Artemov, V. Egorov, M. Debatist, and D. McGinnis, "1300-m-high rising bubbles from mud volcanoes at 2080m in the Black Sea: hydroacoustic characteristics and temporal variability," *Earth Planet. Sci. Lett.*, vol. 244, no. 1–2, pp. 1–15, Apr. 2006.

- [15] C. W. Holland, T. C. Weber, and G. Etiope, "Acoustic scattering from mud volcanoes and carbonate mounds," *J. Acoust. Soc. Am.*, vol. 120, no. 6, p. 3553, 2006.
- [16] S. H. Hickman, P. A. Hsieh, W. D. Mooney, C. B. Enomoto, P. H. Nelson, L. A. Mayer, T. C. Weber, K. Moran, P. B. Flemings, and M. K. McNutt, "Scientific basis for safely shutting in the Macondo Well after the April 20, 2010 Deepwater Horizon blowout," *Proc. Natl. Acad. Sci. U. S. A.*, vol. 109, no. 50, pp. 20268–73, Dec. 2012.
- [17] T. C. Weber, A. De Robertis, S. F. Greenaway, S. Smith, L. Mayer, and G. Rice, "Estimating oil concentration and flow rate with calibrated vessel-mounted acoustic echo sounders," *Proc. Natl. Acad. Sci. U. S. A.*, vol. 109, no. 50, pp. 20240–5, Dec. 2012.
- [18] Ø. Johansen, H. Rye, and C. Cooper, "DeepSpill—field study of a simulated oil and gas blowout in deep water," *Spill Sci. Technol. Bull.*, vol. 8, no. 5–6, pp. 433–443, Jan. 2003.
- [19] C. S. Clay and H. Medwin, *Acoustical oceanography*. New York: John Wiley & Sons, 1977.
- [20] I. R. MacDonald, W. W. Sager, and M. B. Peccini, "Gas hydrate and chemosynthetic biota in mounded bathymetry at mid-slope hydrocarbon seeps: Northern Gulf of Mexico," *Mar. Geol.*, vol. 198, no. 1–2, pp. 133–158, Jun. 2003.
- [21] R. E. Francois and G. R. Garrison, "Sound absorption based on ocean measurements. Part I: pure water and magnesium sulfate contributions," *J. Acoust. Soc. Am.*, vol. 72, no. 3, pp. 896–907, 1982.
- [22] R. E. Francois and G. R. Garrison, "Sound absorption based on ocean measurements. Part II: boric acid contribution and equation for total absorption of sound," *J. Acoust. Soc. Am.*, vol. 72, no. 6, pp. 1879–1890, 1982.
- [23] K. G. Foote, H. P. Knudsen, G. Vestnes, R. Brede, and R. L. Nielsen, "Improved calibration of hydroacoustic equipment with copper spheres," *Int. Counc. Explor. Sea, Fish Capture Comm.*, 1981.
- [24] L. E. Kinsler, A. R. Frey, A. B. Coppens, and J. V. Sanders, *Fundamental of acoustics*, 4th ed. John Wiley & Sons, 2000.
- [25] R. Towler, "readEKRaw EK/ES60 ME/MS70 MATLAB toolkit, rel. 4/16/10," 2010. [Online]. Available: <http://hydroacoustics.net/viewtopic.php?f=36&t=131>. [Accessed: 08-Jul-2011].
- [26] L-3 Communications, "Multibeam sonar theory of operation," 2000. [Online]. Available: <http://www.mbari.org/data/mbsystem/sonarfunction/SeaBeamMultibeamTheoryOperation.pdf>. [Accessed: 09-Jan-2014].
- [27] J. D. Beaudoin, J. E. Hughes Clarke, and J. E. Bartlett, "Application of surface sound speed measurements in post-processing for multi-sector multibeam echosounders," *Int. Hydrogr. Rev.*, vol. 5, no. 3, pp. 17–32, 2004.
- [28] T. C. Weber, K. Jerram, and L. Mayer, "Acoustic sensing of gas seeps in the deep ocean with split-beam echosounders," in *Proceedings of Meetings on Acoustics*, 2012, vol. 17.

- [29] National Oceanic and Atmospheric Administration Office of Coast Survey, "Field procedures manual," 2013. [Online]. Available: [http://www.nauticalcharts.noaa.gov/hsd/fpm/FPM\\_2013\\_Final\\_5\\_3\\_13.pdf](http://www.nauticalcharts.noaa.gov/hsd/fpm/FPM_2013_Final_5_3_13.pdf). [Accessed: 04-Dec-2013].
- [30] Kongsberg Maritime AS, "Seafloor Information System reference manual for EM 122, release 3.8," 2010. [Online]. Available: [ftp://nic2b.whoi.edu/pub/em122/337679ab\\_sis\\_reference\\_manual\\_em122.pdf](ftp://nic2b.whoi.edu/pub/em122/337679ab_sis_reference_manual_em122.pdf). [Accessed: 05-Apr-2011].
- [31] A. Godin, "The calibration of shallow water multibeam echo-sounding systems," University of New Brunswick, 1998.
- [32] W. S. Burdic, *Underwater acoustic system analysis*, 2nd ed. Englewood Cliffs: Prentice Hall, 1991.
- [33] X. Lurton, "Swath bathymetry using phase difference: theoretical analysis of acoustical measurement precision," *IEEE J. Ocean. Eng.*, vol. 25, no. 3, p. 351, 2000.
- [34] I. Leifer and I. MacDonald, "Dynamics of the gas flux from shallow gas hydrate deposits: interaction between oily hydrate bubbles and the oceanic environment," *Earth Planet. Sci. Lett.*, vol. 210, no. 3–4, pp. 411–424, May 2003.
- [35] R. J. Urick, *Principles of underwater sound*, 2nd ed. New York: McGraw-Hill, Inc., 1975.
- [36] D. F. McGinnis, J. Greinert, Y. Artemov, S. E. Beaubien, and a. Wüest, "Fate of rising methane bubbles in stratified waters: How much methane reaches the atmosphere?," *J. Geophys. Res.*, vol. 111, no. C9, p. C09007, 2006.
- [37] G. Rehder, P. W. Brewer, E. T. Peltzer, and G. Friederich, "Enhanced lifetime of methane bubble streams within the deep ocean," *Geophys. Res. Lett.*, vol. 29, no. 15, pp. 21–1–21–4, Aug. 2002.
- [38] L. Chen, E. D. Sloan, C. A. Koh, and A. K. Sum, "Methane hydrate formation and dissociation on suspended gas bubbles in water," *J. Chem. Eng. Data*, 2013.
- [39] P. Tishchenko, C. Hensen, K. Wallmann, and C. S. Wong, "Calculation of the stability and solubility of methane hydrate in seawater," *Chem. Geol.*, vol. 219, no. 1–4, pp. 37–52, Jun. 2005.
- [40] A. V Milkov, R. Sassen, I. Novikova, and E. Mikhailov, "Gas Hydrates at minimum stability water depths in the Gulf of Mexico: significance to geohazard assessment," *Gulf Coast Assoc. Geol. Soc. Trans.*, vol. L, pp. 217–224, 2000.

## APPENDIX

### MATLAB CODE FOR SEEP PROCESSING

The code developed for this research was written using MATLAB and relied upon scripts by Rick Towler (NOAA AFSC) and Dezhang Chu (NOAA NWFSC). The readEKRaw library, developed by Rick Towler and listed in the references, was used to parse Simrad EK60 .all files. Dezhang Chu provided unpublished scripts to estimate the calibration sphere target strength. This appendix includes MATLAB code (on CD) written and used by the author for routine seep detection and processing, as outlined in Figure 10 and detailed in the subsequent list of functions. These files may also be available by request through the University of New Hampshire Center for Coastal and Ocean Mapping. The readEKRaw library and scripts for sphere target strength calculation are included in this appendix, but more recent versions may be available from their authors directly. MATLAB scripts for non-routine data processing steps, such as estimation of transducer angular offsets, modeling of the transducer beam pattern, and creation of figures and tables, are not included but may also be available separately.

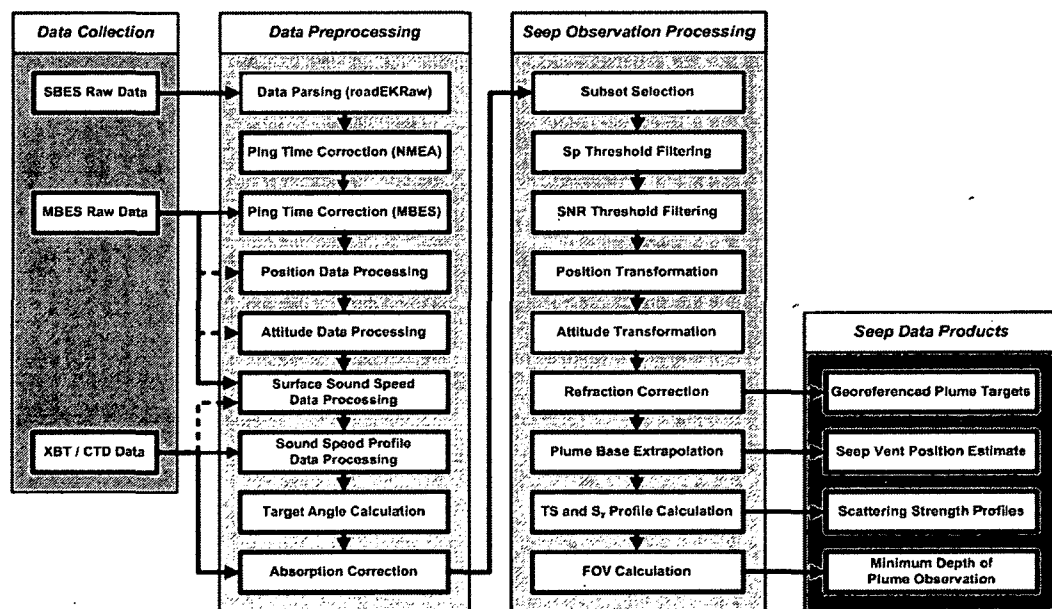


Figure 10. Order of conceptual data processing steps for routine seep detection and characterization, as reflected in the MATLAB code. Steps are grouped into four stages: data collection, data preprocessing, seep observation processing, and creation of seep data products.

The order and indentation of the following list represent the calling order and hierarchy of MATLAB functions for routine seep data processing; for instance, the function at step 1.3 calls the function at 1.3.1.



1. extractSeep\_EK60\_CCOM
  - 1.1. readEKRaw\_CCOM
    - 1.1.1. readEKRaw\_ReadHeader
    - 1.1.2. readEKRaw\_GetSampleCount
    - 1.1.3. readEKRaw\_AllocateSampledata
    - 1.1.4. readEKRaw\_AllocateData
    - 1.1.5. readEKRaw\_ReadDgHeader
    - 1.1.6. readEKRaw\_ParseNMEAstring\_CCOM
    - 1.1.7. readEKRaw\_ReadSampledata
  - 1.2. readEKRaw\_GetCalParms
  - 1.3. readEKRaw\_Power2Sv
    - 1.3.1. readEKRaw\_ConvertPower
  - 1.4. readEKRaw\_Power2Sp
    - 1.4.1. readEKRaw\_ConvertPower
  - 1.5. processTime
  - 1.6. processPingTime
    - 1.6.1. parseEMall
      - 1.6.1.1. parseEMdg\_info
      - 1.6.1.2. parseEMdg78\_rra
      - 1.6.1.3. parseEMdg80\_pos
      - 1.6.1.4. parseEMdg82\_rtp
  - 1.7. processPosition
    - 1.7.1. readEKRaw\_InterpGPS\_CCOM
      - 1.7.1.1. readEKRaw\_DeletePing\_CCOM
      - 1.7.1.2. readEKRaw\_DeleteBot
  - 1.8. processAttitude
  - 1.9. processSoundSpeed
    - 1.9.1. parseASVPorEDF
    - 1.9.2. parseEMsoundspeed
  - 1.10. readEKRaw\_ConvertAngles\_CCOM
  - 1.11. interpOntoSampleTime
  - 1.12. sortAlpha
  - 1.13. applyAlpha
  - 1.14. processSplitBeamData
    - 1.14.1. plotRawData
    - 1.14.2. selectSubset
    - 1.14.3. assignSubset
    - 1.14.4. calcRangeSubset
    - 1.14.5. applyAlphaSubset
    - 1.14.6. filterSubset
    - 1.14.7. filterSubset
    - 1.14.8. maskSubset
    - 1.14.9. calcSNR
    - 1.14.10. processSeepTargs
      - 1.14.10.1. raytraceTargs
      - 1.14.10.2. calcBase
      - 1.14.10.3. calcTS
      - 1.14.10.4. calcProfiles
      - 1.14.10.5. calcFOV
      - 1.14.10.6. plotTargs